TOMOGRAPHY® RESEARCH ARTICLE

GantryMate: A Modular MR-Compatible Assistance System for MR-Guided Needle Interventions

Andreas Reichert[1], Michael Bock[1], Michael Vogele[2], and Axel Joachim Krafft[1]

[1]Department of Radiology, Medical Physics, Medical Center – University of Freiburg, Faculty of Medicine, University of Freiburg, Freiburg, Germany and [2]Interventional Systems GmbH, Kitzbühel, Austria

Corresponding Author:
Andreas Reichert, MSc
Department of Radiology, Medical Physics, Medical Center – University of Freiburg, Killianstr. 5a, 79106 Freiburg;
E-mail: andreas.reichert@uniklinik-freiburg.de

Key Words: interventional magnetic resonance imaging, MR-guided interventional procedures, percutaneous procedures, MRI-compatible assistance system

Abbreviations: Magnetic resonance imaging (MRI), magnetic resonance (MR), phase-only cross-correlation (POCC), gradient-echo (GRE), spin-echo (SE), repetition time (TR), echo time (TE), flip angle (FA), field of view (FOV), bandwidth (BW)

ABSTRACT

Percutaneous minimally invasive interventions are difficult to perform in closed-bore high-field magnetic resonance systems owing to the limited space between magnet and patient. To enable magnetic resonance–guided needle interventions, we combine a small, patient-mounted assistance system with a real-time instrument tracking sequence based on a phase-only cross-correlation algorithm for marker detection. The assistance system uses 2 movable plates to align an external passive marker with the anatomical target structure. The targeting accuracy is measured in phantom experiments, yielding a precision of 1.7 ± 1.0 mm for target depths up to 38 ± 13 mm. In in vivo experiments, the possibility to track and target static and moving structures is demonstrated.

INTRODUCTION

Magnetic resonance imaging (MRI) has unique advantages to guide and monitor interventional procedures over other imaging methods such as computed tomography or ultrasound (US). It offers an unparalleled soft tissue contrast, it can acquire images in arbitrary scan planes along the device trajectories, it provides morphological and functional imaging, and it exposes neither the patient nor the interventionalist to ionizing radiation. MRI can be used at various stages of the intervention—during target localization, device positioning, monitoring of therapeutic progress, and assessment of therapeutic outcome (1-3). Besides intravascular (4) and thermal treatments [e.g., with high-intensity focused ultrasound (5-7)], minimally invasive percutaneous interventions such as needle biopsies tremendously benefit from image guidance (8, 9).

Percutaneous interventional procedures have traditionally been performed in open-bore low-field magnetic resonance (MR) systems to ensure good patient access (10). However, a good contrast-to-noise ratio is required to differentiate the target region from the surrounding tissue, a high signal-to-noise ratio is needed to unambiguously visualize the instruments in the patient's body, and an adequate spatial resolution needs to be ensured to detect, e.g., small deviations from the planned needle pathway. Currently, these requirements are best fulfilled in high-field, high gradient power MRI systems at 1.5 T or 3 T, which are typically constructed as solenoid superconducting MR magnets. However, spatial constraints because of the closed-bore design (typical bore diameter of ≤70 cm, cover-to-cover length in the range of 125–160 cm) limit the physicians' access to the patient and make device handling challenging. Assistance systems can help overcome these problems and facilitate percutaneous interventions (1-3, 11). Such systems have been shown to improve needle placement (12, 13), help to achieve needle trajectories with increased precision, and help to shorten procedure durations (14-17). Any assistance system operating in the MRI environment must not only conform to all conventional safety standards for MRI accessories but also preserve the MR image quality, and its operation has to remain unaffected by the MR system's radiofrequency and magnetic fields. This makes the construction of assistance systems for the MR environment a challenging task.

In recent years, assistance systems have been presented for numerous applications with various degrees of remote control and haptic feedback. The fully MR-compatible pneumatic arm INNOMOTION (18) can hold and align an instrument around a pivot point in 6 degrees of freedom (DOF) over the patient inside the magnet bore. It found only a limited number of applications (19, 20) and is no longer commercially available. Another commercial prototype assistance system is the smaller, second-generation remote-controlled manipulator using pneumatic air stepper motors (21) for MR-guided transrectal prostate biopsies (22). A technically more complex system is the neuroArm (23) driven by ultrasonic piezoelectric motors, which features remotely controlled and exchangeable neurosurgical instruments and provides the neurosurgeon with both visual control and

ISSN 2379-1381 https://doi.org/10.18383/j.tom.2019.00007

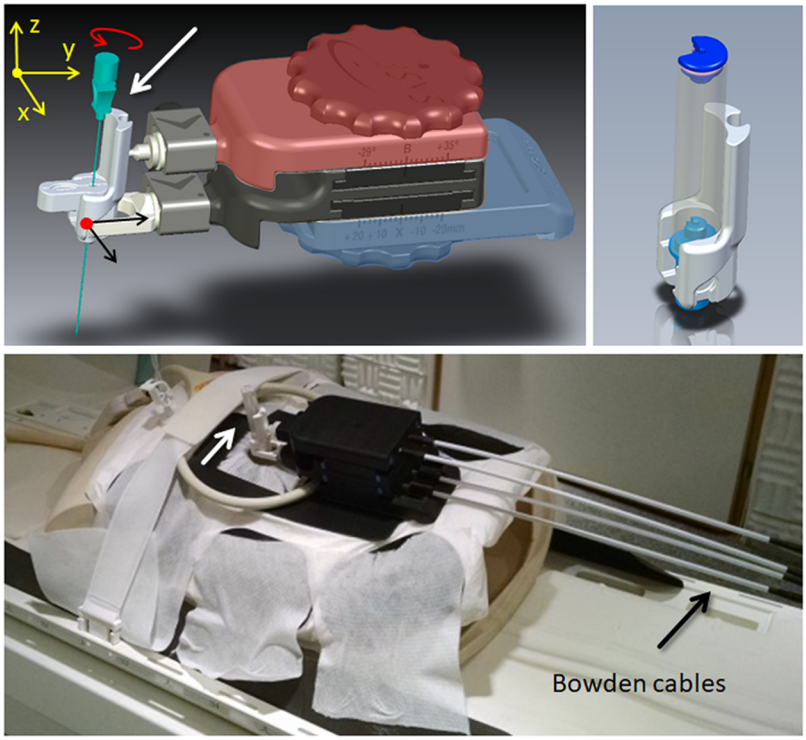

Figure 1. Schematic of the GantryMate assistance system (top, left). The base platform (blue) allows gross positioning of the device, and the upper 2 plates (black and red) can be moved independently in *x* and *y* directions. This allows steering of a distal instrument holder (white arrow) through Bowden cable (visible in the bottom image) from outside the magnet bore. The lower plate (black) translates the instrument holder in *x* or *y* direction, and the upper plate allows for rotations of the holder (red arrow) around a pivot point (red dot). The holder can be equipped with a customized cylindrical marker (top, right) or a needle sleeve (top, left).

haptic feedback. In addition to these commercial systems, several other small patient-mounted systems have been recently presented (13, 24): Monfaredi et al. described a shoulder-mounted robot using 4 MRI-compatible piezo-motors for needle placement with 4 DOF (25). Ghelfi et al. assessed a patient-mounted light puncture robot for percutaneous needle interventions that is fixed to the patient's body to allow for patient movements (26). The 4 piezoelectric driven motors, which are placed at the feet to avoid interferences with MR imaging, enable placement of a needle in 4 DOF through Bowden cables.

Nearly all of these systems depend on sophisticated control mechanisms that require bulky additional hardware in the MR room, making it difficult for them to integrate into the clinical routine (24, 27). Thus, despite the variety and abundance of system designs, only a few of these design concepts were converted into commercially available systems for clinical use (13). Therefore, the exploration and design of novel assistance systems for MR-guided interventions remain areas of active research.

Here, we present an alternative patient-mounted assistance system for image-guided percutaneous needle interventions. Compared with existing systems, this new GantryMate system features a flexible, simpler design and is constructed entirely from plastic material. It can be remotely steered via Bowden cables to manipulate a needle-guide inside the magnet bore, i.e., no additional hardware is required for operation. We tested the assistance system according to American Society for Testing and Materials (ASTM) standards (28-32), and we verified if the MR system's radiofrequency and magnetic fields remain unaffected. To enable automatic scan plane positioning, we combined GantryMate with a tracking MRI sequence to automatically detect a passive marker needle-guide and followed the device motion during targeting in real time (22, 33-35). In a phantom setting, the lateral puncture accuracy of needle placements, as well as the procedure time, was assessed. Furthermore, technical proof of concept in in vivo situations is shown with the successful alignment of the needle pathway with basivertebral veins in the vertebrae and a vessel branch in the liver of a volunteer.

METHODS

Assistance System GantryMate

The assistance system GantryMate (Interventional Systems, Kitzbühel, Austria) is entirely constructed from electrically nonconducting, nonmetallic, and nonmagnetic plastic and fiber glass materials (Figure 1). The system is mounted on a base platform, which is used for gross positioning and can be fixed to the patient with straps. The system consists of 2 movable plates (Figure 1, top left) and an instrument holder, which is attached to the distal end-effector (Figure 1, top right). The plates can each be moved independently in 2 translational DOF (forward-backward—FB, left-right—LR) via 4 mechanical adjustment threads, which are accessible from outside the magnet through Bowden cables (cf. Figure 1, bottom). Manipulation of the lower plate moves the entire unit in either FB or LR direction relative to the base platform (approximate translational range = 40 mm in each direction). Translation (FB and LR direction) of the upper plate relative to the lower plate causes rotations of the distal instrument holder (angular range = ±30° in both directions) about a pivot point located at the level of the lower plate (cf. Figure 1, top left).

During targeting, a passive marker is attached to the instrument holder for online device localization and planning of the needle pathway. Once the marker is correctly aligned with the target in the patient's body, a needle is manually inserted through the marker that now serves as a needle guide, and the

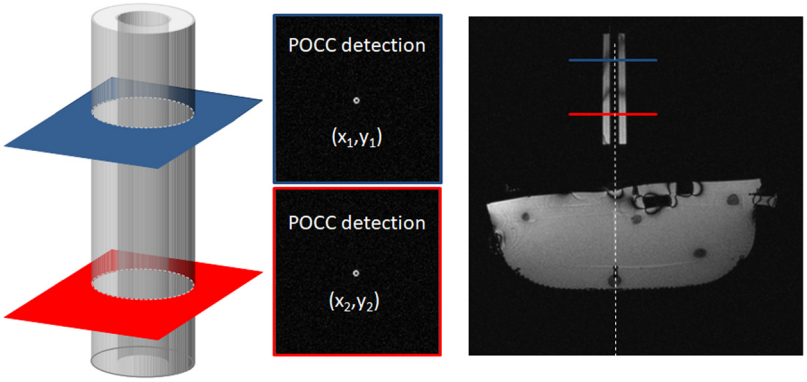

Figure 2. Schematics of the passive marker tracking sequence. Two parallel images (blue and red) are acquired perpendicular to the symmetry axis of the marker (left). The position of the ring-shaped structures can be detected via a POCC algorithm (middle). The position information is used to align a third image along the marker and to visualize the theoretical needle trajectory (right). The sequence runs continuously and allows online needle targeting procedures.

insertion can be visualized with real-time imaging. Alternatively, a needle sleeve can be attached that allows for the use of needles with varying diameters.

Device Tracking

For device tracking during the targeting, the GantryMate system was equipped with a cylindrical passive marker needle-guide (inner/outer diameter = 5/13 mm, length = 62.5 mm) filled with a contrast agent solution (Magnevist®/H_2O: 1/100, Bayer Schering Pharma AG, Berlin, Germany). To automatically determine the position and orientation of the passive marker, a previously developed tracking sequence was used (22, 33-35). The sequence acquires 2 T1-weighted gradient echo (FLASH) images, which are oriented perpendicular to the marker's symmetry axis. In these images, the marker is seen as a ring-like structure (Figure 2) that can be automatically detected via a phase-only cross-correlation (POCC) algorithm (33) during online image reconstruction. Based on the position information, the sequence automatically aligns the plane of a subsequent imaging acquisition with the marker direction. For imaging, a different contrast (balanced steady-state free precession, bSSFP) is used to increase the lesion contrast. The bSSFP image is then displayed online on a screen in the MR room, and the theoretical needle trajectory is overlaid to enable targeting maneuvers of the needle-guide.

MR Safety and Compatibility Measurements

MR experiments were carried out in a 1.5 T whole-body system (MAGNETOM Symphony, Siemens Healthcare, Erlangen, Germany) with a manufacturer-provided open-loop coil (Flex Loop Large, Siemens Healthcare) for signal reception. A bottle (diameter = 12 cm; Siemens Healthcare) filled with a solution [(1.25 g $NiSO_4$ × 6 g H_2O + 5 g NaCl)/1000 g H_2O] was placed on the system's patient table around the magnet's isocenter. Measurements were conducted without and with the assistance system placed on top of the phantom bottle to examine image artifacts and distortions according to the standard ASTM F2119 (30). Therefore, gradient-echo (GRE) and spin-echo (SE) images were acquired in sagittal and axial orientations with the following parameters: GRE: repetition time (TR)/echo time (TE) = 500/15 ms, slice thickness = 3 mm, slices = 20, slice gap = 6 mm, flip angle (FA) = 30°, field of view (FOV) = 350 × 350 mm, matrix = 256 × 256, bandwidth (BW) = 130 Hz/px; SE: TR/TE = 500/20 ms, slice thickness = 5 mm, slices = 20, slice gap = 10 mm, FA = 90°, FOV = 350 × 350 mm, matrix = 256 × 256, BW = 130 Hz/px. Afterwards, a dual-echo GRE sequence was used to assess B_0 distortions without and with the device in place: TR/TE/ΔTE = 15/8.76/4.76 ms, slice thickness = 5 mm, FA = 15°, FOV = 300 × 300 mm, matrix = 256 × 256, BW = 250 Hz/px (Figure 3, left). In addition, 3D GRE images were acquired (TR/TE = 1500/2.6 ms, slice thickness = 1.88 mm, FA = 30/60°, FOV = 127 × 240 mm, matrix = 128 × 68, BW = 279 Hz/px) to assess B_1 distortions and to calculate a relative FA map (Figure 3, right) with the double-angle method (36, 37).

Phantom Measurements

The accuracy of the needle positioning was measured in a phantom experiment with an agar phantom (volume = 50 × 50 × 40 mm^3) with 13 embedded fiducial targets (mean diameter = 8.1 mm), which was placed inside a plastic casing that was shaped like a human torso (Figure 1, bottom). After target definition in a 3D GRE localizer data set, the following procedure, including 4 steps, was performed for each target:

1. The passive marker was attached to the instrument holder at the manipulator's center position.
2. Instrument positioning and alignment of the needle pathway with the target were performed under online guidance with the POCC tracking sequence (Figure 4; FLASH tracking images: TR/TE = 4.0/2.0 ms, FOV = 244 × 300 mm^2, matrix = 156 × 192, α_{FLASH} = 15°, slice thickness = 10 mm, BW = 1180 Hz/px; bSSFP targeting image: TR/TE = 4.0/2.0 ms, FOV = 244 × 300 mm^2, matrix = 156 × 192, α_{bSSFP} = 70°, slice thickness = 5 mm, BW = 1180 Hz/px, TA_{tot} per tracking cycle = 1.9 s).

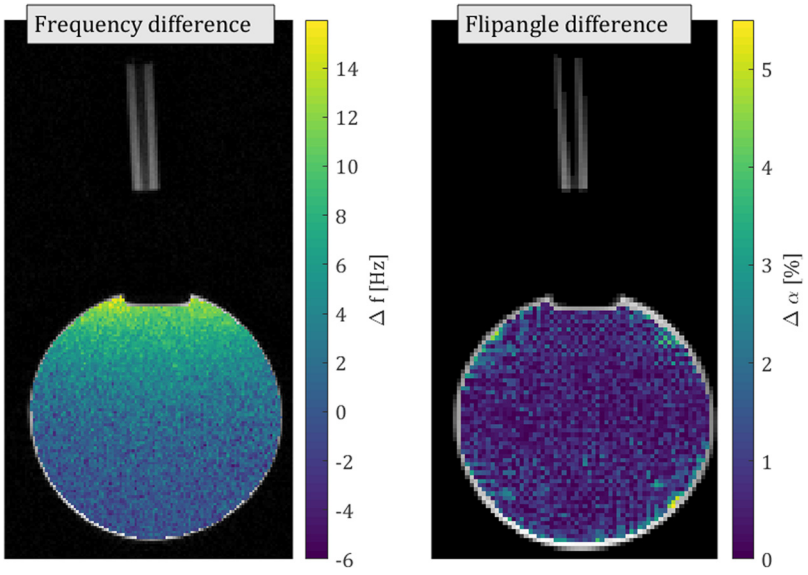

Figure 3. Frequency difference (left) and relative flip angle (FA) difference (right) in the phantom between images acquired before and after the assistance system was placed on the phantom.

3. The passive marker was replaced with a dedicated needle sleeve for a 16-G needle (Somatex GmbH, Teltow, Germany).
4. The needle was manually advanced into the target under online monitoring with a HASTE (*H*alf-Fourier *A*cquisition *S*ingle-shot *T*urbo spin *E*cho imaging) sequence (TR/TE = 2000/46 ms, FOV = 250 × 250 mm^2, matrix = 256 × 256, α_{HASTE} = 180°, thickness = 5 mm, partial Fourier = 4/8, BW = 781 Hz/px).

After all targets were successfully punctured, a high-resolution (0.5 × 0.5 × 0.5 mm^3) 3D bSSFP data set (TR/TE = 7.52/3.76 ms, FOV = 200 × 150 mm^2, matrix = 384 × 288, α_{bSSFP} = 70°, thickness = 0.5 mm, BW = 482 Hz/px) was acquired to evaluate the needle pathways and assess the insertion accuracy. Therefore, the distance of each needle pathway was measured in the gel from the target center using reformatted multiplanar views (Figure 5).

In Vivo Measurements

To simulate an in vivo application, a volunteer was placed on the patient table in supine position, and the assistance system was attached above the abdomen (Figure 6, top left). The assistance system was positioned in its center position, and then a targeting maneuver was simulated using the circular cross sec-

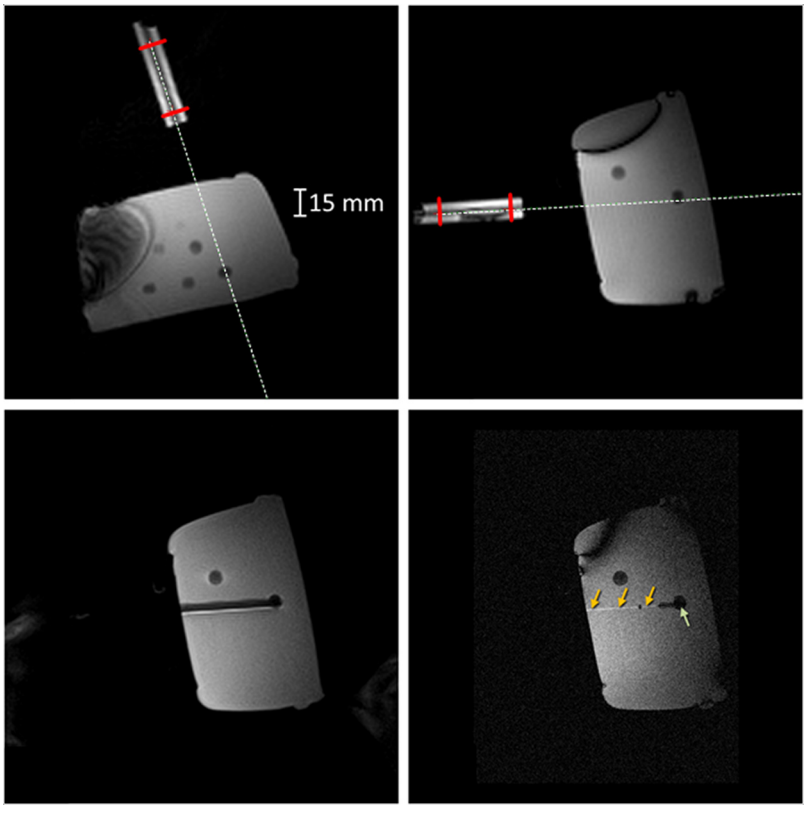

Figure 4. Example of the alignment of the theoretical needle trajectory (dashed white) with the desired target in transversal and sagittal orientation (top left and right). The location of the tracking slices is marked in red. A HASTE sequence is used for online monitoring of the needle insertion (bottom, left). After the needle is removed, the needle pathway (yellow arrows) is visible, which can be used to determine targeting precision (bottom, right).

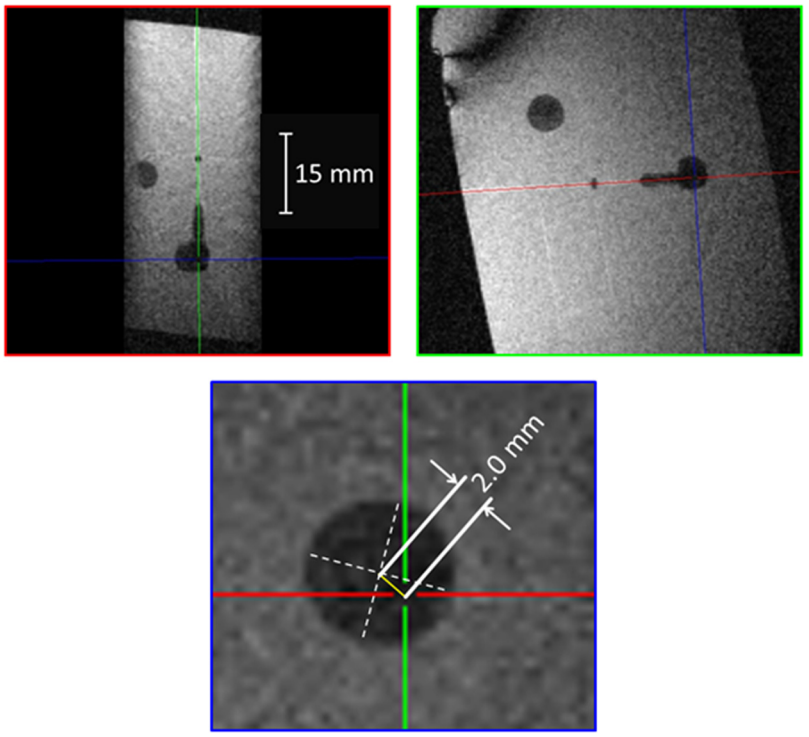

Figure 5. Reformatted orthogonal multiplanar views of the needle pathway (red and green boxes) that define the bullseye-view (blue box) for assessment of the lateral accuracy.

tions of the basivertebral veins in the lumbar vertebra (L2, L3, L4 and L5) as anatomical target structures (Figure 6, top right). The location and orientation of the GantryMate device were manipulated via the Bowden cables under online tracking guidance (FLASH tracking images: TR/TE = 3.6/1.7 ms, FOV: 380 × 380 mm^2, matrix = 154 × 192, α_{FLASH} = 15°, slice thickness = 10 mm, BW = 1042 Hz/px, partial Fourier = 6/8; bSSFP targeting image: TR/TE = 3.6/1.7 ms, FOV: 380 × 380 mm^2, matrix = 154 × 192, α_{bSSFP} = 70°, slice thickness = 5 mm, BW = 1042 Hz/px, partial Fourier = 6/8, TA_{tot} per tracking cycle = 1.3 s) until the needle pathway was aligned with the target in sagittal and transversal views.

To test the assistance system in a moving target, a distal vessel branch of the portal vein was defined as target which is moving over the breathing cycle (Figure 7). Again, the device was manipulated under online tracking guidance until the needle pathway was aligned with the target. Gross alignment was performed during breathing in a transverse view, and final

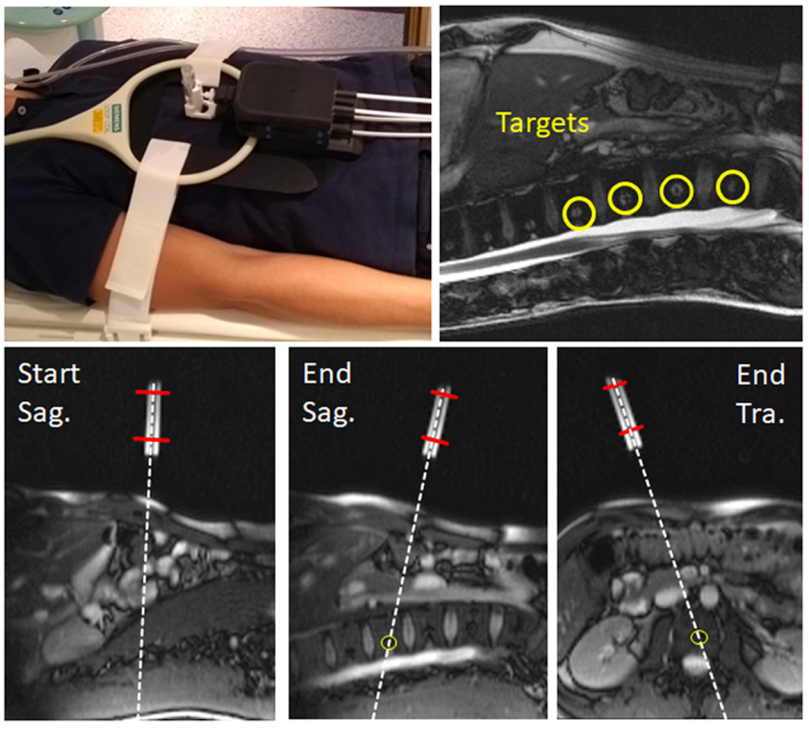

Figure 6. Experimental setup (top left) for the targeting of stationary targets (cross sections of basivertebral veins, top right) in a volunteer. The targeting procedure is started in a sagittal view (bottom left), and the projected needle pathway (dashed white) is aligned with the predefined target region in sagittal and transversal views (yellow circles, bottom middle and right).

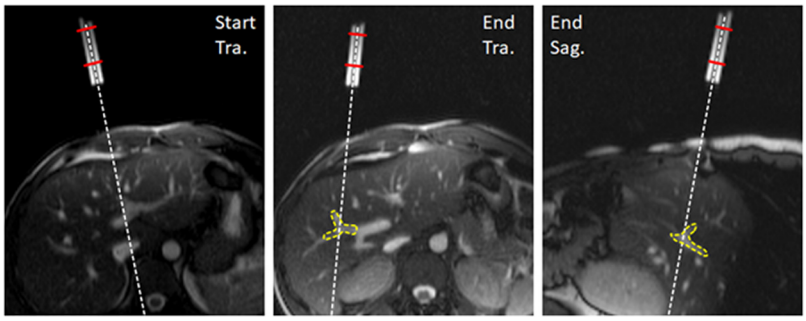

Figure 7. First image of the procedure to align the projected needle pathway (dashed white) with the predefined target region (left). Last images of the procedure in transversal and sagittal view (middle, right); the needle pathway was successfully aligned with the target region.

alignment of the needle pathway was done in a breath-hold maneuver for a sagittal and transverse view.

RESULTS

No distortion or signal loss artifacts were visible in either the GRE or SE images (images not shown). B_0 field and FA mapping without and with the assistance systems revealed no significant influence of the device on either the B_0 or B_1 field, respectively (Figure 3). Here, B_0 maps without and with the setup showed a mean frequency difference of 0.9 Hz, that is, 0.01 ppm (range: −6 and 15.5 Hz). The B_1 field measurements showed almost no effects because of the setup with mean relative B_1 differences of 0.2%.

The results from the needle experiment in the phantom with 13 fiducial targets are summarized in Table 1. Puncturing was successfully performed in all 13 targets within the mean procedure time (duration for instrument positioning, exchange of marker and needle sleeve, and needle insertion) of $t_{puncture}$ = 6.4 ± 1.5 min. The mean lateral distance between the needle channels and the geometric center points of the targets was 1.7 ± 1.0 mm.

In the in vivo experiment, the passive marker needle guide could be successfully aligned with cross sections of the basivertebral veins in the lumbar spine. The durations of the individual targeting procedures are summarized in Table 2 (mean duration for instrument positioning = 2.0 ± 0.5 min). Furthermore, the passive marker needle guide could be also successfully aligned with a moving target in the liver. Here, gross alignment was performed during free breathing (duration = 2.7 min) and final fine alignment could be accomplished during short breath holds for sagittal (duration = 15 s) and transverse (duration = 5 s) image orientation, respectively.

DISCUSSION AND CONCLUSION

In this work, a patient-mounted assistance system for MR-guided needle interventions is presented in combination with an online POCC device tracking sequence. The assistance system is designed to move a passive needle-guide inside of a closed-bore MR system and can be mechanically manipulated from outside the magnet via Bowden cables.

Table 1. Summary of Measured Diameter, Depth from Phantom Surface, Needle Pathway Angles in FB and LR Direction, Duration (Procedure Time for Instrument Positioning and Needle Insertion), and Lateral Distance of Needle Pathway to Target Center for all 13 Targets

Target #	Diameter (mm)	Depth (mm)	Angle FB (°)	Angle LR (°)	Duration (min:second)	Lateral Distance (mm)
1	8.0	53.8	12	16	6:45	1.1
2	8.3	52.9	0	3	4:26	2.0
3	8.1	53.5	16	3	8:46	2.6
4	7.9	53.1	7	3	5:41	3.6
5	7.7	55.9	12	3	7:24	2.6
6	7.5	35.5	17	4	5:59	0.1
7	7.4	33.4	23	1	7:02	1.4
8	8.7	38.4	5	0	6:54	2.3
9	9.0	23.7	28	9	5:27	1.6
10	8.5	23.5	32	19	8:07	0.3
11	8.7	24.2	29	9	8:40	0.7
12	7.8	25.6	16	11	5:01	1.5
13	8.1	20.1	0	0	3:31	2.2
Mean ± SD[a] (range)	8.1 ± 0.5 (7.4–9.0)[a]	38 ± 13 (20.1–55.9)	15 (0–32)	6 (0–19)	6:26 ± 1:33 (3:31–8:46)	1.7 ± 1.0 (0.1–3.6)

[a] Respective mean values and standard deviations (SD) are summarized in the bottom line.

Table 2. Summary of Measured Times of Needle Pathway Alignment with the Vertebral Veins

Lumbar Vertebra	Diameter (mm)	Duration (min:second)
L2	7.7	02:18
L3	9.4	03:03
L4	8.7	01:34
L5	8.2	02:04
L2	7.7	01:55
L3	9.4	01:56
L4	8.7	01:50
L5	8.2	01:36
Mean ± SD[a] (range)	8.6 ± 0.6 (7.7–9.4)	2:00 ± 0:30 (1:34–3:03)

[a] Respective mean values and standard deviations (SD) are summarized in the bottom line.

The assistance system is manufactured from electrically nonconducting, nonmetallic, and nonmagnetic plastic material. Measurements revealed no interference with the magnetic or the radiofrequency fields of the MR system, as can be seen in the small B_0 frequency differences and small relative B_1 distortions (Figure 3). Thus, according to our measurements, the device can be classified as "MR-safe" according to the ASTM F2503 standard (28). This safety assessment is only valid for the holder without the instrument (e.g., a needle), which needs to be tested separately. However, many MR-safe needles are commercially available, which can be used in combination with the assistance system.

In combination with a passive POCC tracking sequence, the assistance system provided an accurate and versatile tool for MR-guided needle interventions. In the phantom measurement, all 13 targets were successfully punctured. The system was intuitive to use, no special training was required, and the surrounding adjacent targets were not unintentionally perforated. The mean procedure duration (6.5 min) and the lateral accuracy (1.7 mm) in this evaluation are comparable to values found in previous studies (22, 33-35).

In the in vivo experiment, the device could target stationary targets such as deep-lying cross sections of the basivertebral veins in the lumbar vertebrae. Here, the needle trajectory could be successfully aligned with the targets in 2.0 ± 0.5 min, which would allow one to perform multiple procedures in a single setting. Furthermore, the device was tested in a moving target—here, a hepatic vessel branch was chosen as a fiducial target because the anatomical structure can be unambiguously identified on MR images—and also follows the movement of the liver during respiratory motion. Again, the targeting procedure could be performed without any special training. Gross targeting could be achieved during breathing motion and fine adjustment with only 2 breath holds in 20 seconds, which is in line with requirements for abdominal procedures.

The current realization of the system allows planning of the lateral needle pathway, whereas the depth of the needle insertion has to be manually defined. For this, the target depth is either predefined in the targeting images before needle insertion. Alternatively, the needle insertion can be monitored continuously using image sequences which are less prone to needle-induced artifacts. Here, real-time monitoring of the insertion has been realized with the spin-echo single-shot technique HASTE, which is insensitive to field inhomogeneities and provides an excellent T2 contrast but is leading to signal saturation and increased specific absorption rate (SAR) values. In this context, accelerated SE-based sequences such as targeted-HASTE (38) were presented for an optimized visualization of the needle insertion. However, in some needle placement scenarios, depth control is not needed. For example, in arthrography contrast agent insertions, the needle is inserted until the tip touches the bone (25).

Currently, targeting the passive marker is not possible as soon as the needle is introduced in the marker because the needle artifacts distort the ring-shaped cross section required for POCC tracking. However, it would be beneficial to place the needle inside of the marker from the very beginning of the procedure because the total procedure time could be reduced as the needle would only have to be mounted once and no exchange of passive marker and needle guide would be required. To enable targeting with the needle inside the marker, again fast spin echo sequences could be used which reduce the needle artifact. Accurate tracking of the marker with the needle in place could be highly advantageous to detect needle deflections from the planned needle trajectory during insertion. Here, the interventionalist could use the direct visual feedback to stabilize the needle trajectory by manual needle rotation (39).

In its current implementation, the device setup with Bowden cables is simpler than that of other assistance systems. Nevertheless, it could be expanded in future for example, with more advanced robotic technologies for fully remote control. With its flexible design, it is not restricted to single interventional scenarios and could be used in many abdominal applications, for example, transgluteal prostate or kidney biopsies. The main components of the device are reusable and only small parts (distal instrument holder, marker, instruments) are made as sterile disposables, which might be important for clinical applicability.

The presented combination of the MR-safe assistance system and online POCC tracking sequence could also be used for other MR-guided interventions. For example, RF ablation electrodes could be placed in the target regions, and the thermal destruction would be subsequently monitored with MR temperature imaging. All these procedures would benefit from acceleration of the POCC tracking sequence. This can be achieved, for example, with simultaneous acquisition of the tracking images (35) or with radially undersampled projection imaging of the passive marker (40). A higher temporal resolution would allow better tracing of anatomical targets during breathing motion.

In conclusion, we presented a simple, accurate, and versatile assistance system in combination with a passive marker tracking sequence, which might be a valuable tool to facilitate MR-guided interventions.

ACKNOWLEDGMENTS

We would like to thank Dr. Florian Maier (Siemens Healthcare, Erlangen, Germany) for support with the implementation of the tracking sequence. Financial support from the Tiroler Innovationsförderung (Project "GantryMate") is gratefully acknowledged. This study was supported by Deutsche Forschungsgemeinschaft (DFG) grant number HA 7006/1-1.

Disclosures: M. Bock reports grants from Tiroler Innovationsförderung (Project "GantryMate") during the conduct of the study; nonfinancial support (research cooperation) from Siemens Healthcare, outside the submitted work. Dr. Vogele reports grants from Tiroler Innovationsförderung, other from Interventional Systems GmbH, during the conduct of the study. In addition, Dr. Vogele has patent 20 2013 007 831 issued to iSYS Medizintechnik GmbH, patent 20 2013 007 831.6 pending to iSYS Medizintechnik GmbH, and patent 20 2011 005 573.6 pending to iSYS Medizintechnik GmbH.

REFERENCES

1. Fritz J, Weiss CR. The state-of-the-art of interventional magnetic resonance imaging: Part 1. Top Magn Reson Imaging. 2018;27(1):1–2.
2. Weiss CR, Fritz J. The state-of-the-art of interventional magnetic resonance imaging: Part 2. Top Magn Reson Imaging. 2018;27:113–114.
3. Kaye EA, Granlund KL, Morris EA, Maybody M, Solomon SB. Closed-bore interventional MRI: percutaneous biopsies and ablations. AJR Am J Roentgenol. 2015; 205:W400–W410.
4. Bock M, Wacker FK. MR-guided intravascular interventions: techniques and applications. J Magn Reson Imaging. 2008;27:326–338.
5. Jolesz FA. MRI-guided focused ultrasound surgery. Annu Rev Med. 2009;60: 417–430.
6. Napoli A, Anzidei M, Ciolina F, Marotta E, Marincola BC, Brachetti G, Mare LD, Cartocci G, Boni F, Noce V, Bertaccini L, Catalano C. MR-guided high-intensity focused ultrasound: current status of an emerging technology. Cardiovasc Intervent Radiol. 2013;36:1190–1203.
7. Yiallouras C, Ioannides K, Dadakova T, Pavlina M, Bock M, Damianou C. Three-axis MR-conditional robot for high-intensity focused ultrasound for treating prostate diseases transrectally. J Ther Ultrasound. 2015;3:2.
8. Beyersdorff D, Winkel A, Hamm B, Lenk S, Loening SA, Taupitz M. MR imaging-guided prostate biopsy with a closed MR unit at 1.5 T: initial results. Radiology. 2005;234:576–581.
9. Overduin CG, Fütterer JJ, Barentsz JO. MRI-guided biopsy for prostate cancer detection: a systematic review of current clinical results. Curr Urol Rep. 2013;14: 209–213.
10. Lewin JS, Petersilge CA, Hatem SF, Duerk JL, Lenz G, Clampitt ME, Williams ML, Kaczynski KR, Lanzieri CF, Wise AL, Haaga JR. Interactive MR imaging-guided biopsy and aspiration with a modified clinical C-arm system. Am J Roentgenol. 1998;170:1593–1601.
11. Weiss CR, Nour SG, Lewin JS. MR-guided biopsy: a review of current techniques and applications. J Magn Reson Imaging. 2008;27:311–325.
12. Heerink WJ, Ruiter SJS, Pennings JP, Lansdorp B, Vliegenthart R, Oudkerk M, de Jong KP. Robotic versus freehand needle positioning in CT-guided ablation of liver tumors: a randomized controlled trial. Radiology. 2019;290:826–832.
13. Arnolli MM, Hanumara NC, Franken M, Brouwer DM, Broeders IA. An overview of systems for CT- and MRI-guided percutaneous needle placement in the thorax and abdomen. Int J Med Robot. 2015;11:458–475.
14. Krieger A, Susil RC, Menard C, Coleman JA, Fichtinger G, Atalar E, Whitcomb LL. Design of a novel MRI compatible manipulator for image guided prostate interventions. IEEE Trans Biomed Eng. 2005;52:306–313.
15. Stoianovici D, Kim C, Srimathveeravalli G, Sebrecht P, Petrisor D, Coleman J, Solomon SB, Hricak H. MRI-safe robot for endorectal prostate biopsy. IEEE ASME Trans Mechatron. 2014;19:1289–1299.
16. Susil RC, Camphausen K, Choyke P, McVeigh ER, Gustafson GS, Ning H, Miller RW, Atalar E, Coleman CN, Ménard C. System for prostate brachytherapy and biopsy in a standard 1.5 T MRI scanner. Magn Reson Med. 2004;52:683–687.
17. Schouten MG, Ansems J, Renema WKJ, Bosboom D, Scheenen TWJ, Fütterer JJ. The accuracy and safety aspects of a novel robotic needle guide manipulator to perform transrectal prostate biopsies. Med Phys. 2010;37:4744–4750.
18. Melzer A, Gutmann B, Remmele T, Wolf R, Lukoscheck A, Bock M, Bardenheuer H, Fischer H. INNOMOTION for Percutaneous Image-Guided Interventions. IEEE Eng Med Biol Mag. 2008;27:66–73.
19. Li M, Kapoory A, Mazilu D, Woody B, Horvath KA. Cardiac interventions under MRI guidance using robotic assistance. In: 2010 IEEE International Conference on Robotics and Automation. 2010. pp. 2574–2579.
20. Miller JG, Li M, Mazilu D, Hunt T, Horvath KA. Robot-assisted real-time magnetic resonance image–guided transcatheter aortic valve replacement. J Thorac Cardiovasc Surg. 2016;151:1407–1412.
21. Bomers JGR, Bosboom DGH, Tigelaar GH, Sabisch J, Fütterer JJ, Yakar D. Feasibility of a 2nd generation MR-compatible manipulator for transrectal prostate biopsy guidance. Eur Radiol. 2017;27:1776–1782.
22. Zamecnik P, Schouten MG, Krafft AJ, Maier F, Schlemmer H-P, Barentsz JO, Bock M, Fütterer JJ. Automated real-time needle-guide tracking for fast 3-T MR-guided transrectal prostate biopsy: a feasibility study. Radiology. 2014;273:879–886.
23. Sutherland GR, Latour I, Greer AD. Integrating an image-guided robot with intraoperative MRI: a review of the design and construction of neuroArm. IEEE Eng Med Biol Mag. 2008;27:59–65.
24. Monfaredi R, Cleary K, Sharma K. MRI robots for needle-based interventions: systems and technology. Ann Biomed Eng. 2018;46:1479–1497.
25. Monfaredi R, Iordachita I, Wilson E, Sze R, Sharma K, Krieger A, Fricke S, Cleary K. Development of a shoulder-mounted robot for MRI-guided needle placement: phantom study. Int J Comput Assist Radiol Surg. 2018;13:1829–1841.
26. Ghelfi J, Moreau-Gaudry A, Hungr N, Fouard C, Véron B, Medici M, Chipon E, Cinquin P, Bricault I. Evaluation of the needle positioning accuracy of a light puncture robot under MRI guidance: results of a clinical trial on healthy volunteers. Cardiovasc Intervent Radiol. 2018;41:1428–1435.
27. Busse H, Kahn T, Moche M. Techniques for interventional MRI guidance in closed-bore systems. Top Magn Reson Imaging. 2018;27(1):9–18.
28. ASTM F2503-13, Standard Practice for Marking Medical Devices and Other Items for Safety in the Magnetic Resonance Environment, ASTM International, West Conshohocken, PA, 2013, www.astm.org [Internet]. ASTM International; Available from: http://www.astm.org/cgi-bin/resolver.cgi?F2503-13; Accessed: April 16, 2019.
29. ASTM F2052-15, Standard Test Method for Measurement of Magnetically Induced Displacement Force on Medical Devices in the Magnetic Resonance Environment, ASTM International, West Conshohocken, PA, 2015, www.astm.org [Internet]. ASTM International; Available from: http://www.astm.org/cgi-bin/resolver.cgi?F2052-15; Accessed: April 16, 2019.
30. ASTM F2119-07(2013), Standard Test Method for Evaluation of MR Image Artifacts from Passive Implants, ASTM International, West Conshohocken, PA, 2013, www.astm.org [Internet]. ASTM International; Available from: http://www.astm.org/cgi-bin/resolver.cgi?F2119-07R13; Accessed: April 16, 2019.
31. ASTM F2182-11a, Standard Test Method for Measurement of Radio Frequency Induced Heating On or Near Passive Implants During Magnetic Resonance Imaging, ASTM International, West Conshohocken, PA, 2011, www.astm.org [Internet]. ASTM International; Available from: http://www.astm.org/cgi-bin/resolver.cgi?F2182-11A; Accessed: April 16, 2019.
32. ASTM F2213-17, Standard Test Method for Measurement of Magnetically Induced Torque on Medical Devices in the Magnetic Resonance Environment, ASTM International, West Conshohocken, PA, 2017, www.astm.org [Internet]. ASTM International; Available from: http://www.astm.org/cgi-bin/resolver.cgi?F2213-17; Accessed: April 16, 2019.
33. de Oliveira A, Rauschenberg J, Beyersdorff D, Semmler W, Bock M. Automatic passive tracking of an endorectal prostate biopsy device using phase-only cross-correlation. Magn Reson Med. 2008;59:1043–1050.
34. Krafft AJ, Zamecnik P, Maier F, de Oliveira A, Hallscheidt P, Schlemmer H-P, Bock M. Passive marker tracking via phase-only cross correlation (POCC) for MR-guided needle interventions: Initial in vivo experience. Phys Med. 2013;29:607–614.
35. Reichert A, Bock M, Reiss S, Overduin CG, Fütterer JJ, Krafft AJ. Simultaneous slice excitation for accelerated passive marker tracking via phase-only cross correlation (POCC) in MR-guided needle interventions. Magn Reson Mater Phys Biol Med. 2018;31:781–788.
36. Stollberger R, Wach P. Imaging of the active B1 field in vivo. Magn Reson Med. 1996;35:246–251.
37. Cunningham CH, Pauly JM, Nayak KS. Saturated double-angle method for rapid B1+ mapping. Magn Reson Med. 2006;55:1326–1333.
38. Zimmermann H, Müller S, Gutmann B, Bardenheuer H, Melzer A, Umathum R, Nitz W, Semmler W, Bock M. Targeted-HASTE imaging with automated device tracking for MR-guided needle interventions in closed-bore MR systems. Magn Reson Med. 2006;56:481–488.
39. Abolhassani N, Patel R, Moallem M. Needle insertion into soft tissue: a survey. Med Eng Phys. 2007;29:413–431.
40. Reichert A, Krafft AJ, Bock M. Passive marker tracking with phase-only cross correlation (POCC) in highly undersampled radial images: improvements by point-spread-function considerations. In: Proceedings of the International Society of Magnetic Resonance in Medicine (ISMRM); 2018; Paris, France.